

## Research Article

# On the Use of Compound and Extracted Models in Thermal Dosimetry Assessment

Mario Cvetković <sup>1</sup>, Hrvoje Dodig <sup>2</sup>, and Dragan Poljak <sup>1</sup>

<sup>1</sup>Faculty of Electrical Engineering, Mechanical Engineering and Naval Architecture, University of Split, R. Boskovića 32, 21000 Split, Croatia

<sup>2</sup>Faculty of Maritime Studies, University of Split, R. Boskovića 37, 21000 Split, Croatia

Correspondence should be addressed to Mario Cvetković; [mcvetkov@fesb.hr](mailto:mcvetkov@fesb.hr)

Received 27 May 2020; Revised 20 July 2020; Accepted 28 July 2020; Published 17 August 2020

Academic Editor: Nunzio Salerno

Copyright © 2020 Mario Cvetković et al. This is an open access article distributed under the Creative Commons Attribution License, which permits unrestricted use, distribution, and reproduction in any medium, provided the original work is properly cited.

This paper deals with thermal analysis of realistic models of the human eye and brain using the finite element method. The research presented in this paper is the sequel to the electromagnetic dosimetry model presented in the previous work by the authors. The paper presents the numerical results for the specific absorption rate (SAR) and the related temperature increase in various models of the human eye and the brain/head exposed to high-frequency (HF) electromagnetic (EM) radiation. Based on the numerical results for the induced electric field, the distribution of SAR in the human brain and human eye is determined, subsequently used as input to the thermal model. The thermal dosimetry model of both the brain and eye are based on the form of Pennes' bioheat transfer equation, numerically solved using the finite element method (FEM). The comparison between the extracted models and the compound models of both the eye and brain, placed inside the realistic head model is presented. In case of the human eye, generally, comparable results were obtained for both SAR and temperature increase, while the compound eye model is found to be more suitable when the polarization of incident wave is considered. Moreover, the extracted eye model underestimated the temperature rise, attributed to better heat exchange than the compound model. The results for the compound eye indicate that in some situations, the eye lens could be omitted from simulation, facilitating the model preparation. The numerical results for all three brain models showed similar distributions of SAR and temperature rise. Also, the obtained results show that the peak SAR does not exceed the basic restriction limit for localized SAR, for occupational exposure. The thermal dosimetry assessment of the human brain exposed in four considered scenarios indicates the temperature should not exceed 0.1°C. Finally, the use of a geometrically simplified model may also be found useful in the initial dosimetry assessment prior to dealing with models with more anatomical features.

## 1. Introduction

The proliferation of mobile technology in the last couple decades has increased the number of high-frequency electromagnetic (EM) sources present in the human environment. This also resulted in the raised concern among the general population related to the possible harmful effects, due to fields generated by various wireless communication equipment. The established biological effect of high-frequency (HF) electromagnetic fields is tissue heating [1], due to EM energy absorbed by the biological body. The main goal of HF dosimetry is to quantify the thermal effects, i.e., to

assess the level and distribution of the electromagnetic energy absorbed by the body. The basic dosimetric quantity for the assessment of HF exposure is based on determining the specific absorption rate (SAR) that is related to the electric field induced in the tissue. As the experimental measurements on humans in the high dose range or for long-term exposures are not possible, the computational models based on the numerical solution are used as a tool for assessment of HF exposure [2–5].

The computational models utilized in this type of assessment range from the simplified models, computationally much less demanding but failing to provide accurate results

in most of the exposure scenarios [6] to realistic models of the human body (or particular organs of interest) based on the magnetic resonance imaging (MRI) (e.g., [7–9]).

The anatomically precise models of the complete human body are nowadays available (e.g., [10, 11]); however, modeling the detailed human body requires the knowledge of various tissue parameters, while at the same time, significantly burdening the model preparation phase and straining the available computational resources later. The first issue is common to computational analysis of the complex biological system, such as the brain or eye, and is related to the uncertainties of various input parameters that can result in uncertainties in the assessment of the related scenarios [12]. To overcome this problem, the recently used approach is to couple the deterministic model with certain statistical methods, such as stochastic collocation method (SCM) [12] or generalized polynomial chaos (gPC) [13], to name only a few.

However, the other issue in the simulation of the complex biological system, addressed in this work, is the question of the geometrical representation of the organ, i.e., the accuracy of the model itself. Although, nowadays, very detailed anatomically correct models, obtained using the MRI, are available, the preparation of such a model can often be a tedious work. The use of a detailed model could lead to long computational time and could raise the memory requirements necessary to run these simulations, preventing the application of optimization techniques or the statistical methods [12, 13], where a large number of simulations are often necessary [14]. In addition to this, there are cases when only the particular organ or body parts are of a research interest, or when the initial assessment is considered. The selection between the simplified single organ model and the more detailed and complete body model is no simple task.

This paper is a follow-up to study [15], on the use of the compound and the extracted brain and eye models, in high-frequency electromagnetic exposure assessment. The study in [15] analysed the numerical results of the induced electric field obtained using the hybrid finite element method/boundary element method (FEM/BEM) formulation and the surface integral equation- (SIE-) based formulation and the associated method of moments solution, respectively. The results for the induced electric field presented in [15] are used as inputs to thermal dosimetry assessment presented in this paper. Several different scenarios, featuring the human eye and brain models ranging from the single-tissue one to models having many anatomical details, exposed to HF electromagnetic radiation at different frequencies and different polarizations are considered.

This work aims to clarify if the use of geometrically more simpler models such as the three-compartment model, or even the homogeneous model, lacking many of the anatomical features present in the compound model, could be found useful in the rapid thermal dosimetry assessment, and if the results of these initial assessments could be used later with more elaborate models.

The paper is organized as follows. The description of the extracted and the compound eye and brain models, respectively, are given in the first part. The brief description of

two electromagnetic models is given, followed by the description of thermal dosimetry models and the corresponding numerical solution using the finite element method (FEM). The numerical results for the specific absorption rate (SAR) and the resultant temperature rise in two different eye models and three different brain models, respectively, exposed to plane EM wave of different frequencies and polarizations are given in the following section. The discussion of the results is also given, followed by the concluding remarks given in the final part.

## 2. Materials and Methods

*2.1. Human Eye and Head Models.* Two models have been developed to investigate how the addition of extra tissues affects the distribution of the specific absorption rate (SAR) and the resulting temperature increase inside the human eye.

The first model, termed the extracted, or the single eye model, has been developed from the available MRI scans and the medical measurements data [16], consisting of 16 ocular tissues, as shown in Figure 1.

The thermal parameters of the extracted eye model and the tissue mass density  $\rho$ , used in the thermal dosimetry assessment, are given in Table 1.

The extracted eye model is placed in the homogeneous surrounding region, i.e., air, and although this situation could not be considered a realistic one, it could be useful to assess the effects of adding the surrounding head tissues.

The second model, termed the “compound eye model,” represents the extracted model incorporated in the full human head model, consisting of additional tissues, as shown in Figure 2(c)). This full human head model is later also used in the comparison between several head/brain models.

The three human brain models of varying degrees of complexity, related to the number of tissues included and the level of details pertaining to geometrical details, have been developed. These include the homogeneous model, the three-compartment model, and the compound model, respectively, as shown in Figure 2.

Geometrically the least complex model, consisting of only one tissue, shown in Figure 2(a)), is the so-called homogenised realistic-shaped brain reported in [17]. This model is a very simple representation of the human brain, scaled to average brain dimensions of length 167 mm, width 140 mm, height 93 mm, and volume  $1400 \text{ cm}^3$  [18].

The parameters of the homogeneous human brain are taken as the average values between the white and grey matter, as shown in Table 2. The electrical properties of the tissue are considered as linear and isotropic, according to [17].

Although this model is geometrically more realistic than the sphere, it lacks the detailed cortical structures and inclusion of additional tissues such as grey/white matter and ventricles. Nonetheless, this homogeneous model has been recognised as useful in the initial assessment comparison [19].

The surface of this model was discretized using 696 triangular elements, while the interior domain is discretized using 1871 tetrahedral elements, using the existing triangles as their boundary faces.

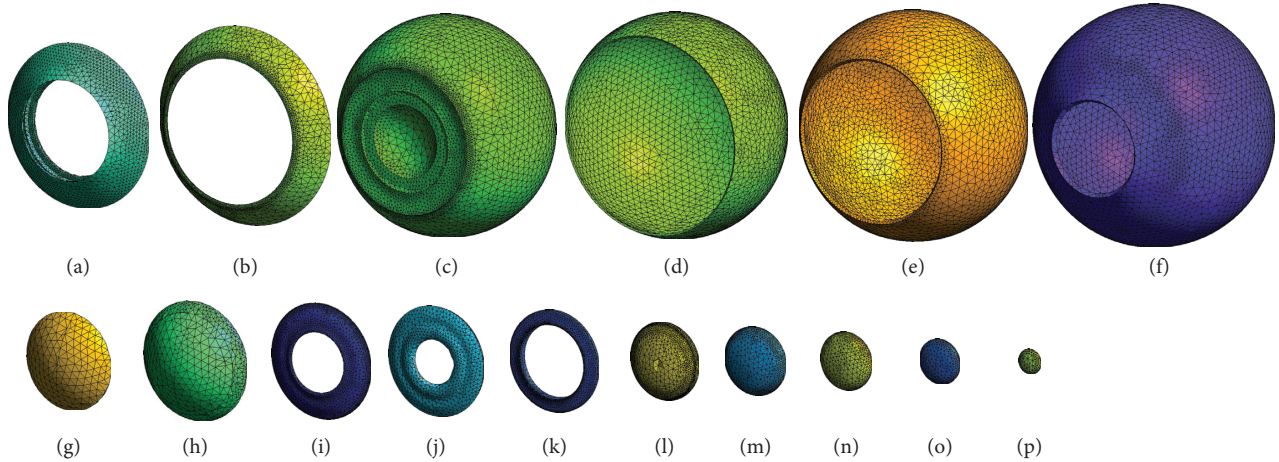


FIGURE 1: Modeled tissues from the extracted and the compound eye models (from [15]). (a) Ciliary body. (b) Ora serrata. (c) Vitreous humour. (d) Retina. (e) Choroid. (f) Sclera. (g) Cornea. (h) Aqueous humour. (i) Posterior ligaments. (j) Iris. (k) Ligaments. (l) Lens-I. (m) Lens-II. (n) Lens-III. (o) Lens-IV. (p) Lens-V.

TABLE 1: Tissue parameters used in eye and head thermal dosimetry models.

Tissue	$\rho$ (g/m <sup>3</sup> )	$c_b$ (J/kg/°C)	$\lambda$ (W/m/°C)	$W_b$ (W/m <sup>3</sup> /°C)	$Q_m$ (W/m <sup>3</sup> )
Brainstem	1043	3600	0.503	35000	10000
Cerebellum	1039	3680	0.565	35000	10000
Head skin	1050	3500	0.420	9100	1000
Liquor	1035	3840	0.530	0	0
Skull	1900	1300	0.300	1000	0
Mandible	1900	1300	0.300	1000	0
Grey matter	1039	3680	0.565	35000	10000
Anterior chamber	1003	3900	0.580	0	0
Choroid	1060	3840	0.530	0	0
Ciliary body	1040	3430	0.498	2700	690
Cornea	1076	4200	0.580	0	0
Iris	1040	3430	0.498	2700	690
Ligaments	1040	3300	0.420	2700	690
Ora serrata	920	2500	0.250	520	180
Posterior chamber	1000	3997	0.578	0	0
Retina	1039	3680	0.565	35000	10000
Sclera	1170	4200	0.580	13500	0
Vitreous body	1009	3997	0.594	0	0
Lens-I	1100	3000	0.400	0	0
Lens-II	1100	3000	0.400	0	0
Lens-III	1100	3000	0.400	0	0
Lens-IV	1100	3000	0.400	0	0
Lens-V	1100	3000	0.400	0	0

The second model, consisting of two additional tissues surrounding the brain, namely, skull and scalp, is termed the “three-compartment head model,” as depicted in Figure 2(b). This model represents the increase in the level of detail, compared to the homogeneous one. The 3-compartment (3-shell) model is the realistic head representation routinely used in experimental magnetoencephalography (MEG) [20] and recently in deterministic-stochastic EM dosimetry [21].

This model is also freely available and can be easily implemented in the BEM analysis [20]. The parameters of the three-shell model, consisting of homogeneous compartments of the brain, skull, and scalp, are given in Table 2.

Finally, the detailed model of the human head, constructed from the MRI of a 24-year-old male [22], is used in this work. The current implementation of the model features 7 additional head tissues in addition to ocular tissues used in the extracted eye model. The head tissue parameters used in the brain thermal dosimetry model are given in Table 1.

**2.2. Electromagnetic Dosimetry Models.** The distribution of SAR inside the human body generally depends on the parameters of the exposed body, but also on the incident electromagnetic (EM) field. In order to find SAR, it is first necessary to determine the corresponding electric field distribution inside the biological body.

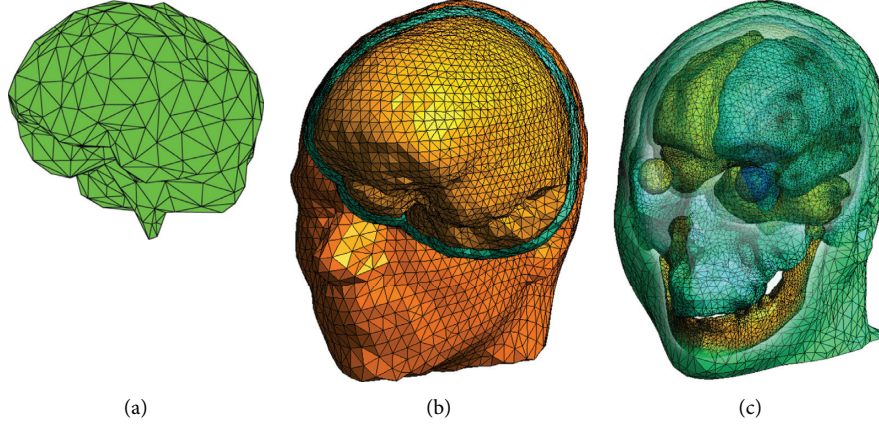


FIGURE 2: Models for the brain comparison: (a) homogeneous brain model, (b) three-compartment head model, and (c) compound model. Overlay on two latter models is showing various head tissues surrounding the brain (from [15]).

TABLE 2: Thermal parameters used in the three-compartment model and homogeneous model.

Tissue	$\rho$ (g/m <sup>3</sup> )	$c_b$ (J/kg/°C)	$\lambda$ (W/m/°C)	$W_b$ (W/m <sup>3</sup> /°C)	$Q_m$ (W/m <sup>3</sup> )
Scalp	1050	3600	0.498	35000	690
Brain	1039	3640	0.534	2700	10000
Skull	1900	1300	0.300	1000	0
Hom. model	1046	3500	0.513	33297	6385

The two models for the high-frequency EM exposure assessment used in this work are previously reported in [15] and, for the sake of the completeness, are outlined in this section. Namely, the numerical results for the induced electric field distribution are obtained using the hybrid finite element method/boundary element method (FEM/BEM) formulation and the electric field integral equation (EFIE) formulation based on the use of the moment method [15].

The plane EM wave incident on the human head or the eye representing an unbounded scattering problem can be formulated using the Stratton–Chu formula, where the time harmonic electric field in the exterior region can be expressed using the following boundary integral equation [23, 24]:

$$\alpha \vec{E}'_{\text{ext}} = \vec{E}'_{\text{inc}} + \oint_{\partial V} \hat{n} \times (\nabla \times \vec{E}_{\text{ext}}) G dS + \oint_{\partial V} \left[ (\hat{n} \times \vec{E}_{\text{ext}}) \times \nabla G + (\hat{n} \cdot \vec{E}_{\text{ext}}) \nabla G \right] dS, \quad (1)$$

where  $\hat{n}$  is an outer normal to surface  $\partial V$  bounding the volume  $V$  and  $\alpha$  is the solid angle subtended at the observation point. The total electric field in the exterior domain

and the known incident electric field are denoted by  $\vec{E}_{\text{ext}}$  and  $\vec{E}_{\text{inc}}$ , respectively, and the free space Green's function  $G$  is given by

$$G = G(\vec{r}, \vec{r}') \frac{e^{-jkR}}{4\pi R}; \quad R = |\vec{r}, \vec{r}'|, \quad (2)$$

where  $R$  is the distance between the observation and the source point and  $k$  is the free space wave number.

The interior inhomogeneous domain is governed by the vector Helmholtz equation, given by

$$\nabla \times \left( \frac{j}{\omega\mu} \nabla \times \vec{E}_{\text{int}} \right) - (\sigma + j\omega\epsilon) \vec{E}_{\text{int}} = 0. \quad (3)$$

The details on the coupling between interior and exterior regions and numerical treatment of the above hybrid formulation can be found elsewhere (e.g., [15, 23]).

The electromagnetic exposure assessment for the case of a homogeneous model can be estimated using the surface integral equation (SIE) formulation [25, 26]:

$$j\omega\mu_n \iint_S \vec{J}(\vec{r}) G_n(\vec{r}, \vec{r}') dS' - \frac{j}{\omega\epsilon_n} \iint_S \nabla'_S \cdot \vec{J}(\vec{r}) \nabla G_n(\vec{r}, \vec{r}') dS' + \iint_S \vec{M}(\vec{r}) \times \nabla' G_n(\vec{r}, \vec{r}') dS' = \begin{cases} \vec{E}^{\text{inc}} & n = 1, \\ 0 & n = 2 \end{cases} \quad (4)$$

where  $\vec{J}$  and  $\vec{M}$  are the equivalent electric and magnetic current densities, respectively,  $k_n$  is the wave number of the interior/exterior region ( $n = 1, 2$ ), and  $G_n$  is the Green function for the homogeneous interior/exterior domain [25, 26].

More details on the procedure can be found elsewhere (e.g., in [25, 26]).

**2.3. Thermal Dosimetry Model.** The governing equation for the steady-state heat transfer in biological tissues is given by the Pennes bioheat equation [27]:

$$\nabla \cdot (\lambda \nabla T) + W_b c_b (T_a - T) + Q_m + Q_{\text{ext}} = 0, \quad (5)$$

where  $Q_m$  represents the generated heat due to metabolic processes,  $W_b$  and  $c_b$  are the volumetric perfusion rate and the specific heat capacity of blood, respectively,  $\lambda$  is the tissue thermal conductivity, and  $T_a$  is the temperature of arterial blood.

Thermal parameters of various human eye and head tissues are given in Table 1.

The last term in (5) represents the external source, e.g., electromagnetic power deposited in the biological body, i.e., the heat generated per unit time and per unit volume due to absorbed EM energy, and can be obtained using

$$Q_{\text{ext}} = \rho \cdot \text{SAR}, \quad (6)$$

where  $\rho$  is the tissue density given in Table 1.

The specific absorption rate (SAR) from (7), given in W/kg, represents the standard measure in thermal dosimetry and can be readily found using

$$\text{SAR} = \frac{\sigma}{2\rho} |\vec{E}|^2, \quad (7)$$

where  $\sigma$  is the conductivity of particular biological tissue, while  $E$  represents the peak value of the electric field induced inside the body obtained from the electromagnetic dosimetry model [15].

Since the analytical solution of (6) is possible only for canonical geometries, the problem of determining the temperature distribution in the human head and eye models is addressed numerically. The finite element method is used in this paper, while the boundary element method approach could also be employed, such as in [5, 28].

The boundary conditions for bioheat equation (6) are either of a Dirichlet and/or Neumann type imposed on the boundary surface of the model, which in latter case is given by

$$\lambda \frac{\partial T}{\partial \vec{n}} = -h(T - T_{\text{amb}}), \quad (8)$$

where  $h$  is the convection coefficient between the surface and the surroundings and  $T_{\text{amb}}$  denotes the ambient temperature.

In case of human eye models, the selected values for the convection coefficient were  $h_c = 20 \text{ W/m}^2\text{C}$ , at the interface between the eye and the air, and  $h_c = 40 \text{ W/m}^2\text{C}$ , at the interface between the eye and the surrounding tissue, respectively, taken from [29].

On the other hand, the widely used value for the human head heat transfer coefficient is  $h_c = 40 \text{ W/m}^2\text{C}$ , while for the homogeneous brain model, the so-called effective coefficient can be used [30], with a typical value of  $h_{\text{eff}} = 12 \text{ W/m}^2\text{C}$  for the human brain, according to [31].

Finally, the present implementation of the thermal dosimetry model neglects the heat transfer (loss) by radiation and the forced convection, respectively.

**2.4. FEM Solution.** The finite element formulation of (5) is based on the weighted residual approach, as in [30]. For the sake of completeness, only the outlines of the mentioned technique are given in the following section, while more complete explanation could be found in [30].

The approximate solution of (5) is expanded using the known basis functions and the unknown coefficients, followed by multiplication of (5) by a set of weighting functions and integrating over the problem domain.

After some work, the suitable expression for the finite element method is obtained:

$$\begin{aligned} \int_{\Omega} \lambda \nabla T \cdot \nabla W_j d\Omega + \int_{\Omega} W_b T W_j d\Omega + \int_{\partial\Omega} h T W_j dS = \\ = \int_{\Omega} (W_b T_a + Q_m + Q_{\text{ext}}) W_j d\Omega + \int_{\partial\Omega} h T_{\text{amb}} W_j dS. \end{aligned} \quad (9)$$

Implementing the Galerkin–Bubnov procedure and subsequently by the standard finite element discretization of (11), the weak formulation for the finite element domain  $\Omega_e$  is obtained, written in matrix form as

$$[K]^e \{T\}^e = \{M\}^e + \{P\}^e, \quad (10)$$

where  $[K]^e$  is the finite element matrix,

$$[K]_{ji}^e = \int_{\Omega_e} \lambda^e \nabla W_i \cdot \nabla W_j d\Omega_e + \int_{\Omega_e} W_b^e W_i W_j d\Omega_e, \quad (11)$$

$\{M\}^e$  is the flux vector on the boundary  $\partial\Omega_e$  of the finite element,

$$\{M\}_j^e = \int_{\partial\Omega_e} \lambda^e \frac{\partial T}{\partial \vec{n}} W_j dS_e, \quad (12)$$

and  $\{P\}^e$  is the finite element source vector,

$$\{P\}_j^e = \int_{\Omega_e} (W_b^e T_a + Q_m^e + Q_{\text{ext}}^e) W_j d\Omega_e, \quad (13)$$

respectively.

Solving (11)–(13) for each of the  $N$  tetrahedral elements, the global matrix is assembled from the contribution of the local finite element matrices, while the global flux and the source vectors are assembled from the local flux and the local source vectors, respectively:

$$[K]\{T\} = \{M\} + \{P\}, \quad (14)$$

where the elements of vector  $T$  are the temperature values at nodes representing the vertices of tetrahedra used to discretize the problem domain.

### 3. Results and Discussion

#### 3.1. Results for the Human Eye Models

**3.1.1. Specific Absorption Rate.** The first set of numerical results is presented for the two human eye models, the extracted and the compound models, respectively. The plane EM wave of 1 GHz and 1.8 GHz is considered, both horizontally and vertically polarized, incident on the eye corneal surface, perpendicular to the coronal head/eye cross section. The amplitude of the incident EM wave is normalized to 1 V/m. The results for the electric field induced in two eye models are obtained using the hybrid FEM/BEM formulation, and could be found in a previous paper [15].

The results obtained using the hybrid FEM/BEM approach were compared to the previous investigations based on the use of an established FDTD method [32, 33]. The comparison of eye-averaged SAR at 1.5 GHz for two polarizations can be found in Table 3.

As seen from Table 3, satisfactory agreement between the two methods has been found. Small difference in the compared results could be attributed to difference in the human eye modeling such as different number of tissues used and the discretization of MRI images into elements. This is evident even when the same method (FDTD) is employed [32].

The specific absorption rate (SAR) is determined from (7) using the calculated electric field distribution and the tissue densities reported in Table 1. The surface distribution of SAR at two frequencies of interest, obtained using the extracted and the compound eye models, respectively, are given in Figures 3(a) and 3(b) for the incident wave of 1 GHz and in Figure 4 for the incident wave of 1.8 GHz (Figures 4(a) and 4(b)), used in our country for GSM.

From Figures 3 and 4, the uneven surface distribution of SAR is evident. Using the extracted eye model, the symmetrical distributions, as well as similar maximum values, are obtained at both frequencies. In this case, the only difference was obviously due to different polarizations of the incident wave, compared to the compound eye model where it was not observed. This could be attributed to the additional tissues surrounding the cornea and sclera.

Furthermore, the appearance of several noncontiguous areas suggest that additional mesh refinement should be performed in these regions, where the very thin layers of several tissues (cornea, aqueous, ligaments, iris, and ciliary body) are closely arranged. This imposes additional work in already tedious preparation of model geometry of organ delicate such as the human eye. On the other hand, it should be noted that the results reported in this work are not additionally postprocessed, such as often is the case when an additional smoothing procedure is implemented [19].

Compared to the SAR results for the incident wave of 1 GHz, the results for 1.8 GHz obtained using the extracted eye model, depicted in Figure 4(a), show that the maximum SAR value is obtained in the eye interior tissues. This is consistent with a previous study [24] which showed that in the frequency range from 1 to 2 GHz, the absorbed electromagnetic energy is concentrated around the lens tissue.

TABLE 3: Comparison of eye-averaged SAR at 1.5 GHz, with a power density of 5.0 mW/cm<sup>2</sup>.

SAR (W/kg)	Hybrid BEM/FEM	FDTD [32]	FDTD [33]
HPol	1.37	1.25	1.5
VPol	1.47	1.5	Not reported

HPol and VPol denote horizontal polarization and vertical polarization, respectively.

The distribution of the induced SAR in the transverse cross section of the two eye models could be found in [29].

In addition to preceding qualitative comparison of the SAR surface distribution, more details on the distribution of the induced SAR inside the two eye models can be seen on Figure 5, where the results for SAR distribution along the eye visual axis is shown.

The results for both models show similar distribution trends along the pupillary axis, with the extracted model showing three times higher SAR values at 1.8 GHz, than the compound model, obtained in the vitreous humour region posterior to the lens. The compound model, on the other hand, showed the double increase of SAR in the posterior vitreous region at vertically polarized 1 GHz wave, while at horizontal polarization, the obtained values are comparative for both models.

Similar to results for the electric field along the eye axis, reported in a previous paper [15], the SAR axial distribution in the extracted eye model shows overlapping graphs for both polarizations at the particular frequency of the incident wave. As a result, the axially symmetrical extracted eye model does not differentiate between the two linear polarizations, as suggested in [15].

From Figure 5, it is also interesting to note the decrease in the SAR value (and the electric field) in the eye lens for both models, with more clearly pronounced effect at 1 GHz, than at 1.8 GHz. The results suggest that although the lens dampens the SAR in the lens itself, it does not significantly affect the distribution in adjacent tissues, suggesting it could be beneficial in model preparation if the lens tissues are omitted. This might be useful in cases when we are interested in the deposition of EM energy in the anterior (superficial) eye regions; such is the case at frequencies related to 5G technology [34]. Further analysis should be carried out to investigate this result.

**3.1.2. Temperature Distribution.** To determine the temperature rise due to absorbed EM energy, the initial temperature distribution is calculated first. The comparison of the initial temperature distribution in the extracted and compound models, respectively, is reported in [5, 29, 35].

The following set of the results are related to temperature increase in the two human eye models due to EM radiation exposure. The numerical solution to Pennes bioheat equation is obtained using FEM outlined in the previous section. The SAR results from the electromagnetic dosimetry model are used as input to the thermal dosimetry model.

The surface distribution of temperature increase at two frequencies of interest, obtained using the extracted and the

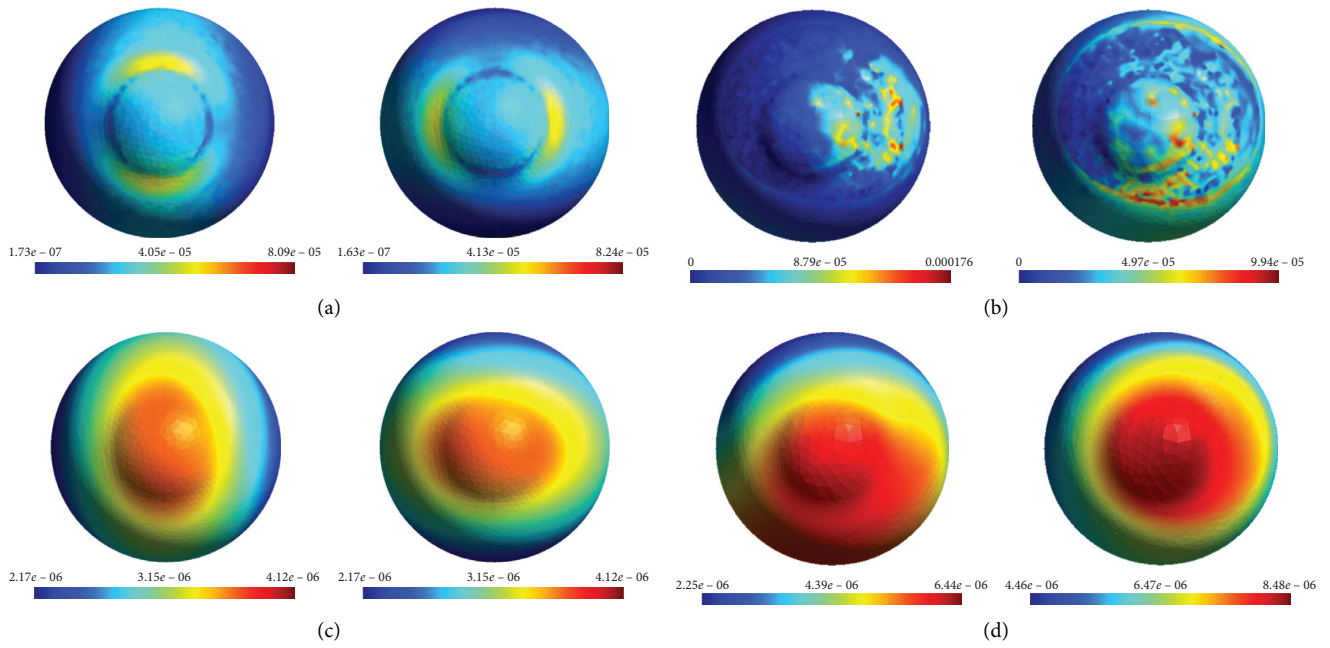


FIGURE 3: Surface distribution of SAR (in W/kg) (a, b) and temperature increase (in °C) (c, d) due to 1 GHz EM wave. Results obtained using the extracted eye model are in the top row and the compound eye model are in the bottom row. In each figure, the results on the left are due to horizontal polarization and on the right are due to vertical polarization.

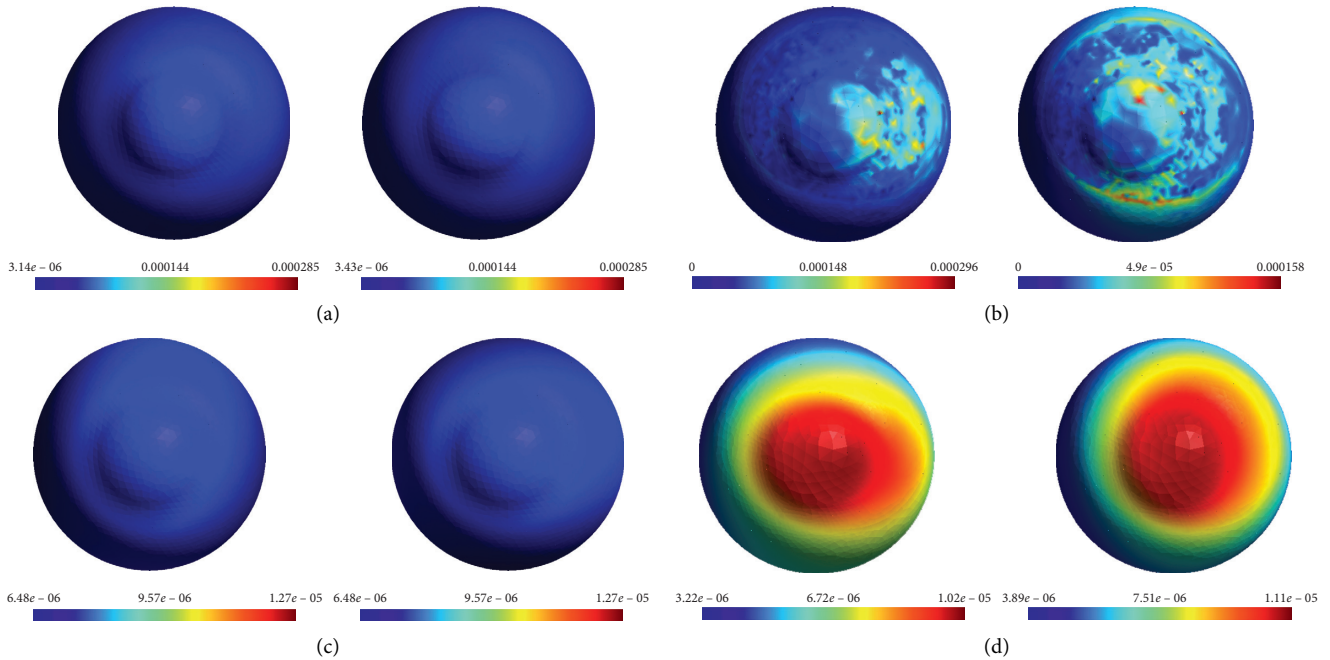


FIGURE 4: Surface distribution of SAR (in W/kg) (a, b), and temperature increase (in °C) (c, d) due to 1.8 GHz EM wave. Results obtained using the extracted eye model are in the top row and the compound eye model are in the bottom row. In each figure, the results on the left are due to horizontal polarization and on the right are due to vertical polarization.

compound eye models, respectively, is given in Figures 3(c) and 3(d) for the incident wave of 1 GHz, and in Figures 4(c) and 4(d) , for the incident wave of 1.8 GHz.

As expected, the results for the extracted eye model show symmetrical distribution, while in the case of the compound model, due to heat exchange between the eye and the

surrounding tissues, the region with maximum temperature rise will be shifted downward and outward, respectively, depending on the polarization of the incident wave. Moreover, the extracted eye model results show lower temperature rise, due to temperature of the ambient air being set to 20°C, than the compound model where the eye is

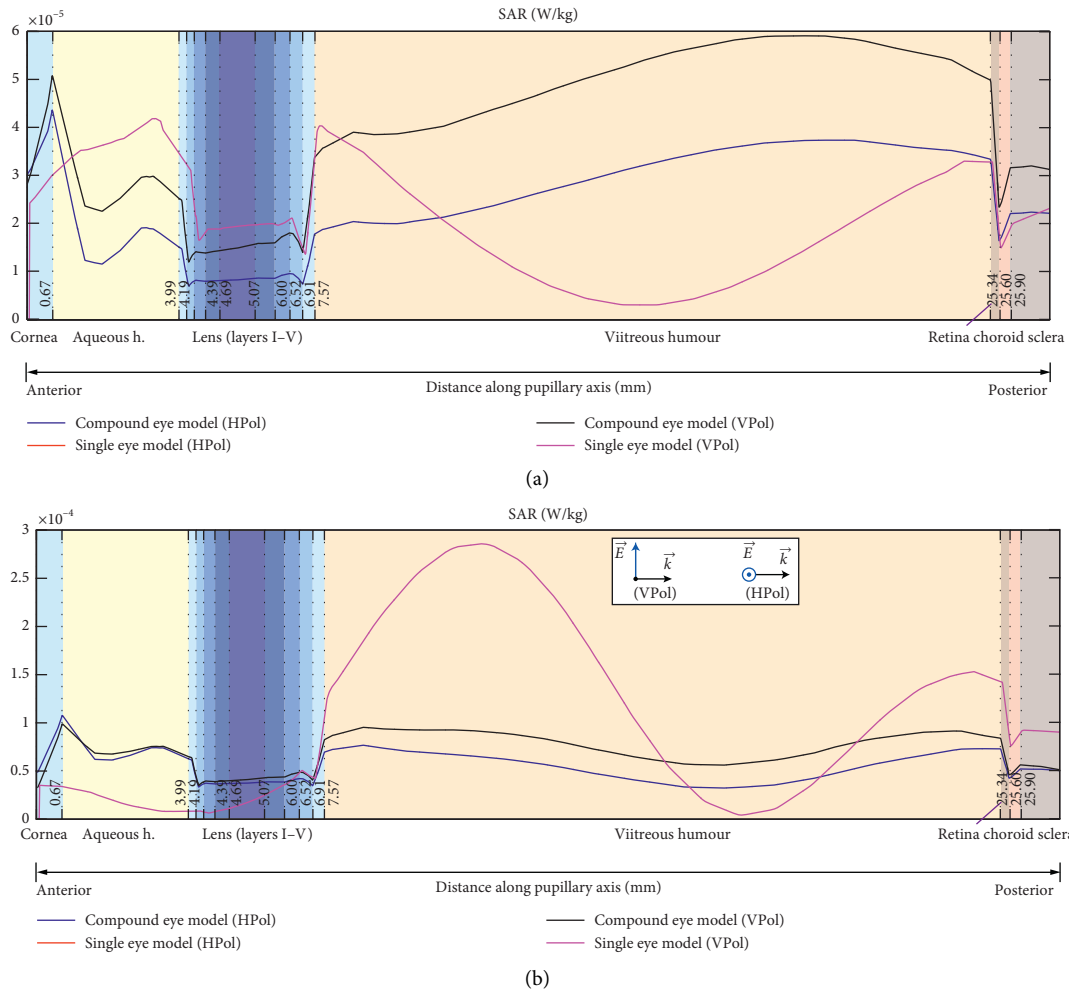


FIGURE 5: Comparison of the SAR distribution along the pupillary axis of the compound and the extracted eye models, respectively, for both polarizations of the incident wave at (a) 1 GHz and (b) 1.8 GHz.

surrounded by the tissues perfused by blood whose temperature is set to  $36.7^{\circ}\text{C}$ .

More details on the temperature increase along the eye visual axis can be seen in Figure 6.

As evident from Figure 6, the steady decrease of the temperature rise from the corneal region to the retina and sclera are obtained using the compound model. The extracted model results, on the other hand, show increase in the temperature rise from the cornea to the anterior part of the vitreous region, followed by steady decrease towards the posterior regions.

Moreover, as seen in Figure 6, practically identical results along the eye visual axis are obtained for both vertical and horizontal polarizations, respectively, at both considered frequencies. On the other hand, the compound model results show similar trends; however, somewhat higher values were achieved in case of vertical polarization than in case of horizontal one.

**3.2. Results for the Human Brain Models.** Our previous paper [15] reported the numerical results for the induced electric field in the homogeneous, 3-compartment, and compound models,

respectively, obtained using SIE/MoM and hybrid FEM/BEM formulations. Those results are used in this paper to determine the specific absorption rate, as reported in the following.

**3.2.1. Specific Absorption Rate in Different Human Brain Models.** Four different situations were considered, related to human brain/head exposed to EM wave, of both vertical and horizontal polarizations, with frequencies of 900 MHz and 1.8 GHz, respectively, and the incident wave-normalized amplitude in each case was set to 1 V/m. The incident plane wave was directed perpendicular to the anterior part of the brain/head models.

The distribution of SAR on the brain surfaces of the homogeneous model, the three-compartment model, and the compound model, respectively, are given in Figures 7–10.

From Figures 7–10, similar surface distributions of SAR are evident in the latter two models, while the distribution in the homogeneous model is differing mainly in the lower model regions where the very sharp geometry representing the brainstem is present, compared to other two more elaborate models, where the brainstem is not present.

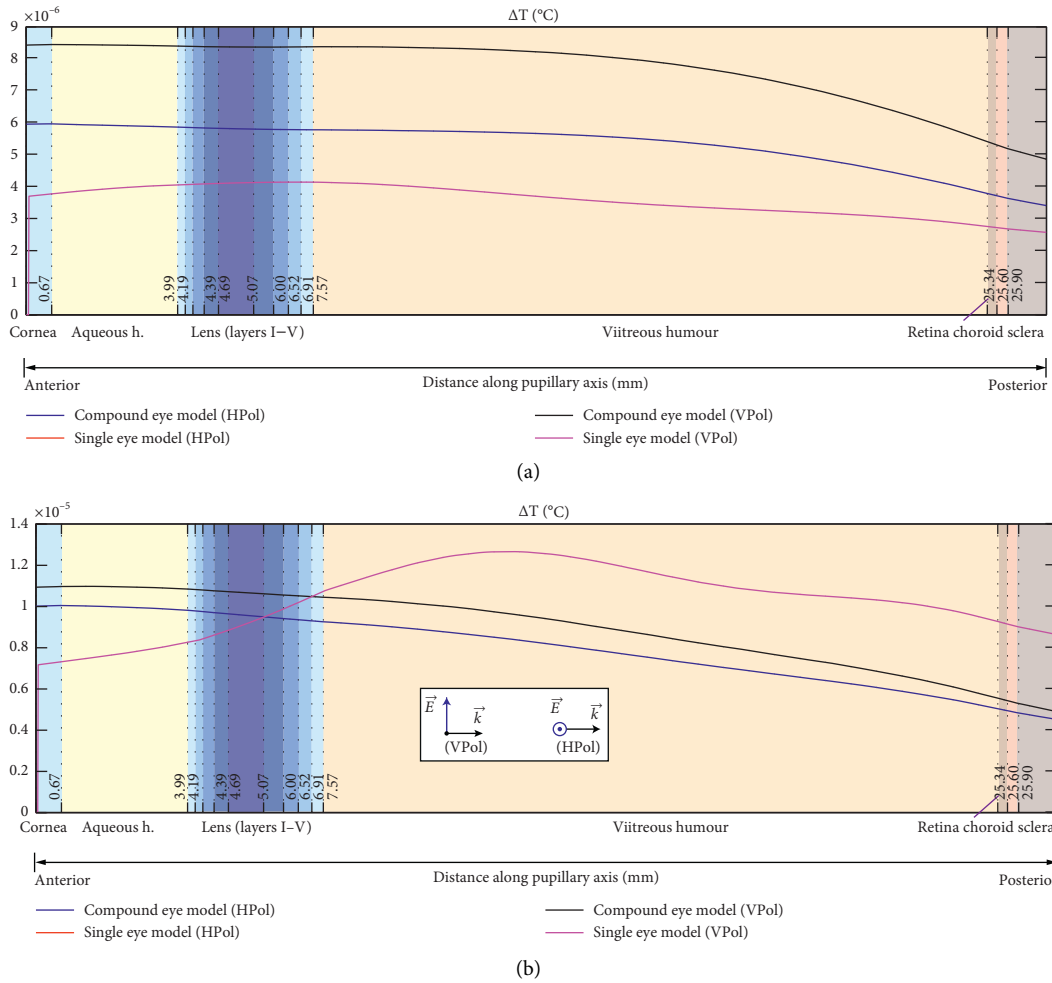


FIGURE 6: Comparison of the temperature increase along the pupillary axis of the compound and the extracted eye models, respectively, for both polarizations of the incident wave at (a) 1 GHz and (b) 1.8 GHz.

As shown by the colormaps, the lower maximum values of SAR (in W/kg) were obtained in all four cases in the homogeneous brain model than other two brain models.

As the value of incident electric field is normalized to 1 V/m, the above results could be scaled in order to compare the obtained values with studies from [1, 36]. In case of 1 V/m electric field, the corresponding equivalent power density is  $P = 1.326 \text{ mW/m}^2$ , while  $5 \text{ mW/cm}^2$ , i.e.,  $50 \text{ W/m}^2$ , is the value of the equivalent plane wave power density representing the worst case used as the reference level ( $f/40$ ) set for that particular frequency ( $f$ ) [1, 36]. This scaling results in the value of incident electric field to reach 194.16 V/m, according to [30], and SAR can be scaled according to (7). Table 4 gives the results for the scaled peak SAR values (W/kg), for three brain models.

The calculated results show that the peak SAR value obtained in all three human brain models does not exceed the limit set by the ICNIRP [1, 36] as a basic restriction for localized SAR (in the head and the trunk), for the occupational exposure (10 W/kg).

More details on the distribution of SAR along the sagittal axis of three different brain models are given in

Figures 11–14. The results are obtained on the perpendicular line starting approximately from the medial prefrontal cortex. Mostly, similar distributions are obtained with all three models, with two elaborate models showing stronger peaks at interior and/or posterior parts where additional tissues such as skull and skin are present and, at the same time, being omitted in the single-tissue model.

In the area corresponding to the grey matter, in all four exposure scenarios, the compound model obtained higher values, than other two models. In this same region, at 900 MHz, the homogeneous model showed very uniform SAR distribution, compared to other models. However, it is interesting to note the distribution at 1.8 GHz in case of the homogeneous model having very similar trend not only in the central part of the brain but also along the whole inspected line.

3.2.2. *Temperature Increase in Different Human Brain Models.* The final set of the results are related to temperature increase obtained using the three head/brain models. The numerical results obtained by means of FEM are given in Figures 15–22.

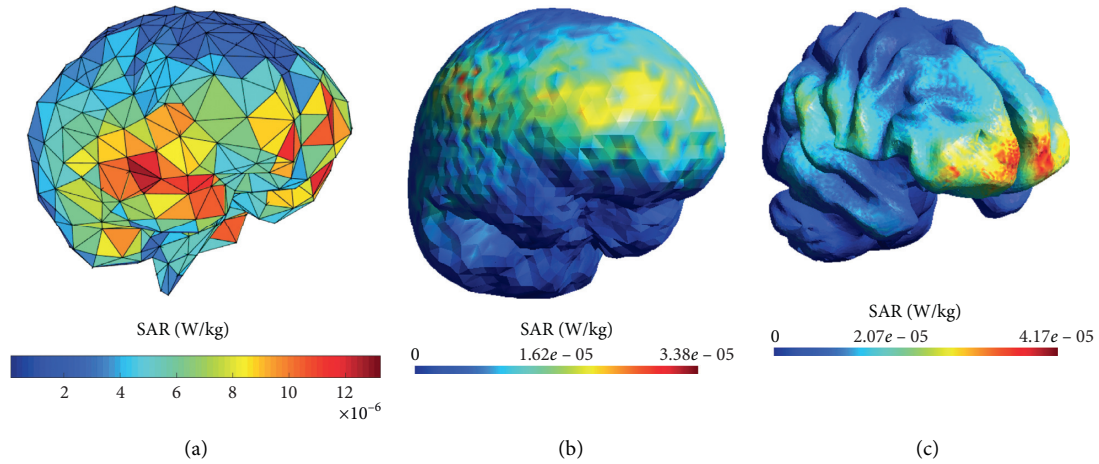


FIGURE 7: Distribution of SAR on the brain surface due to 900 MHz horizontally polarized EM wave: (a) homogeneous model, (b) three-compartment model, and (c) compound model.

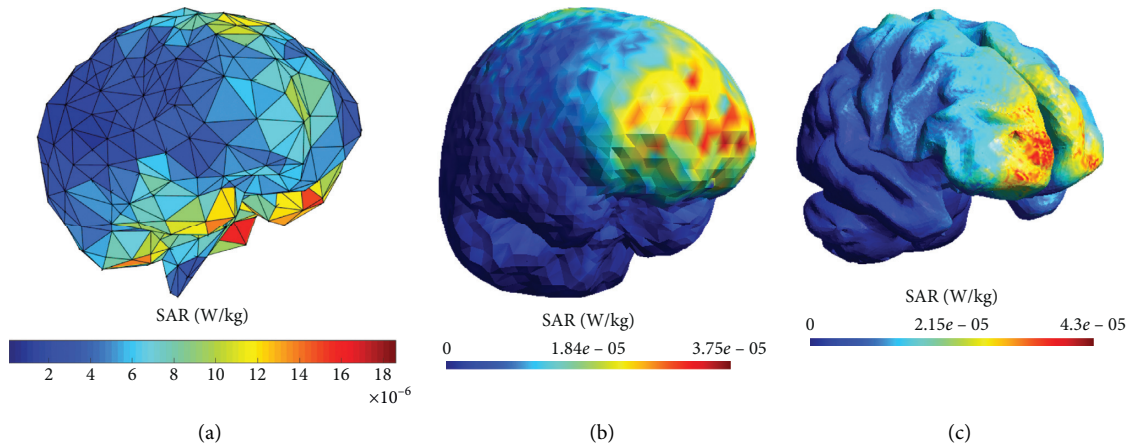


FIGURE 8: Distribution of SAR on the brain surface due to 900 MHz vertically polarized EM wave: (a) homogeneous model, (b) three-compartment model, and (c) compound model.

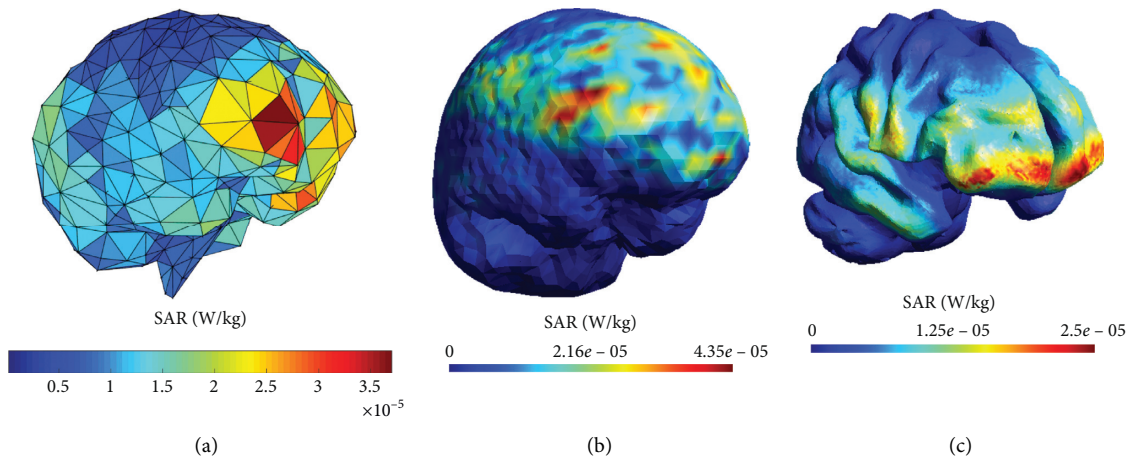


FIGURE 9: Distribution of SAR on the brain surface due to 1.8 GHz horizontally polarized EM wave: (a) homogeneous model, (b) three-compartment model, and (c) compound model.

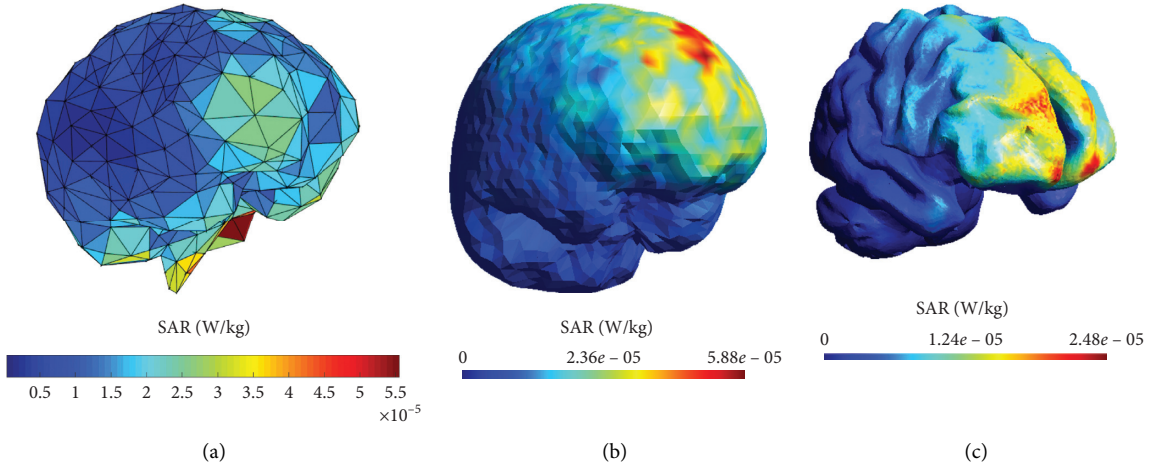


FIGURE 10: Distribution of SAR on the brain surface due to 1.8 GHz vertically polarized EM wave: (a) homogeneous model, (b) three-compartment model, and (c) compound model.

TABLE 4: Peak SAR value (W/kg) scaled using incident power density of  $5 \text{ mW/cm}^2$  and corresponding  $Q_{\text{sar}}$  ( $\text{W/m}^3$ ) for three different models.

	Freq.(MHz), pol.	900, HP	900, VP	1800, HP	1800, VP
<i>Hom. model</i>	$\text{SAR}_{\text{max}}$	0.498	0.716	1.395	2.073
	$Q_{\text{sar}}$	521	749	1459	2169
<i>3-layered m.</i>	$\text{SAR}_{\text{max}}$	1.274	1.414	1.640	2.217
	$Q_{\text{sar}}$	1333	1479	1715	2319
<i>Compound m.</i>	$\text{SAR}_{\text{max}}$	1.572	1.621	0.942	0.935
	$Q_{\text{sar}}$	1644	1696	986	978

HP and VP denote horizontal polarization and vertical polarization, respectively.

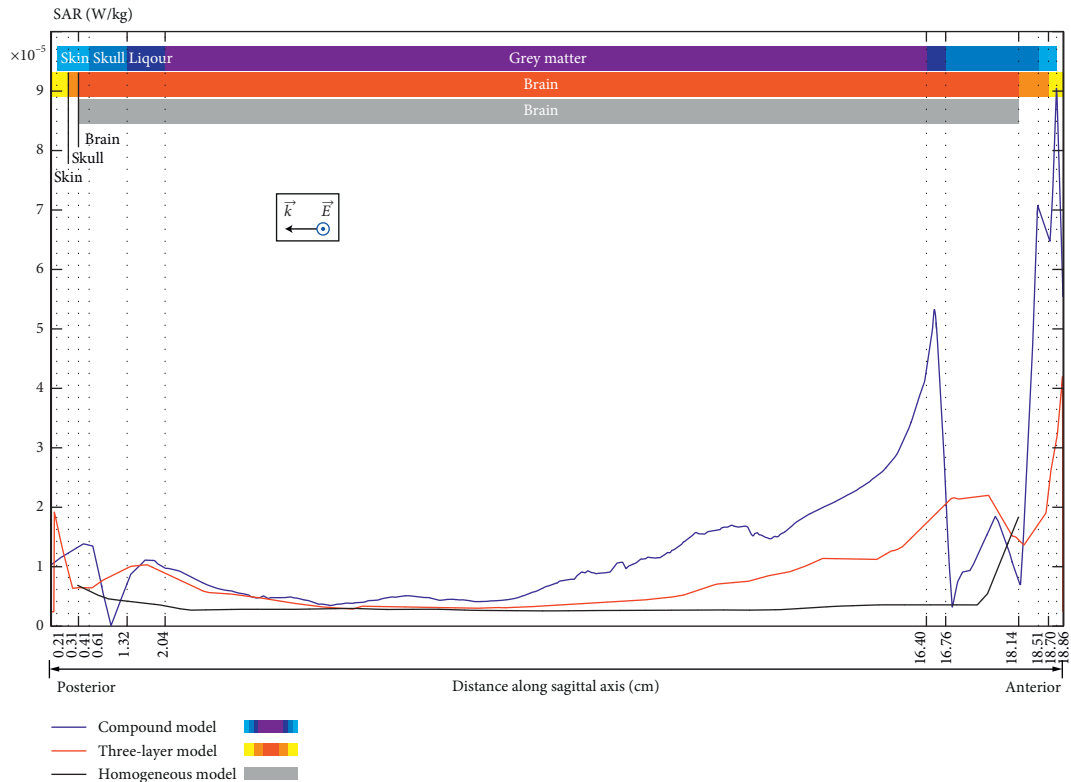


FIGURE 11: Comparison of the induced SAR along the sagittal axis of the homogeneous, the three-compartment, and the compound models, respectively, due to 900 MHz EM wave, horizontal polarization, incident on the anterior side.

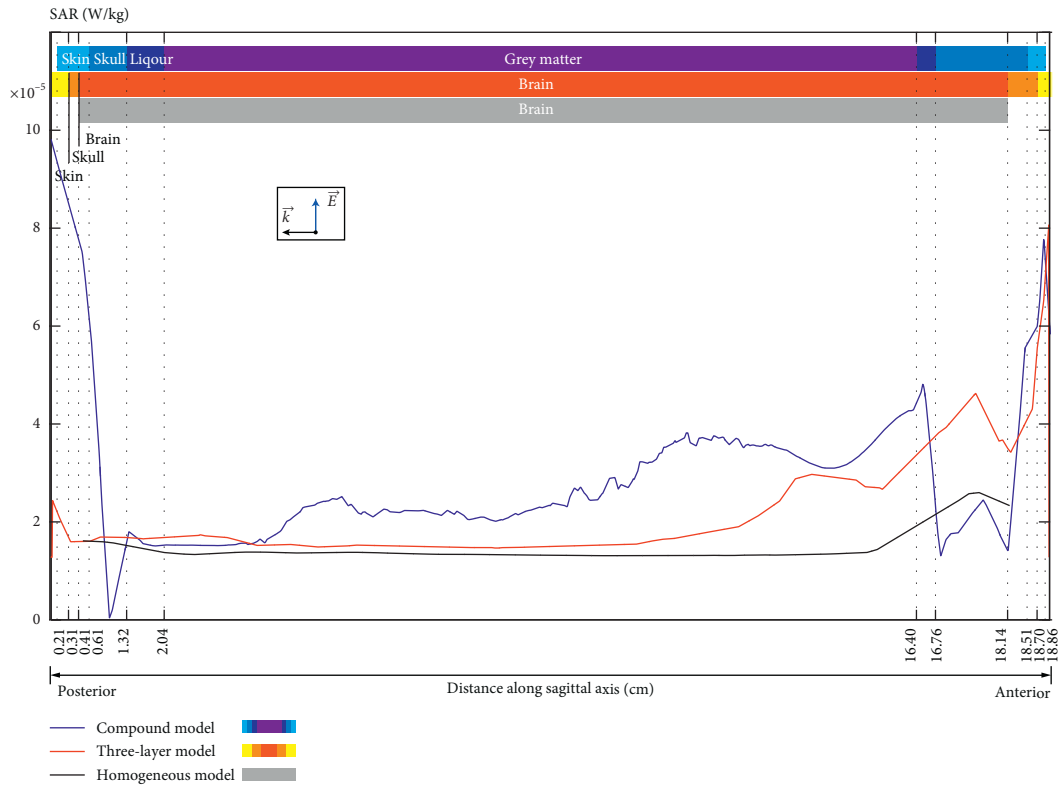


FIGURE 12: Comparison of the induced SAR along the sagittal axis of the homogeneous, the three-compartment, and the compound models, respectively, due to 900 MHz EM wave, vertical polarization, incident on the anterior side.

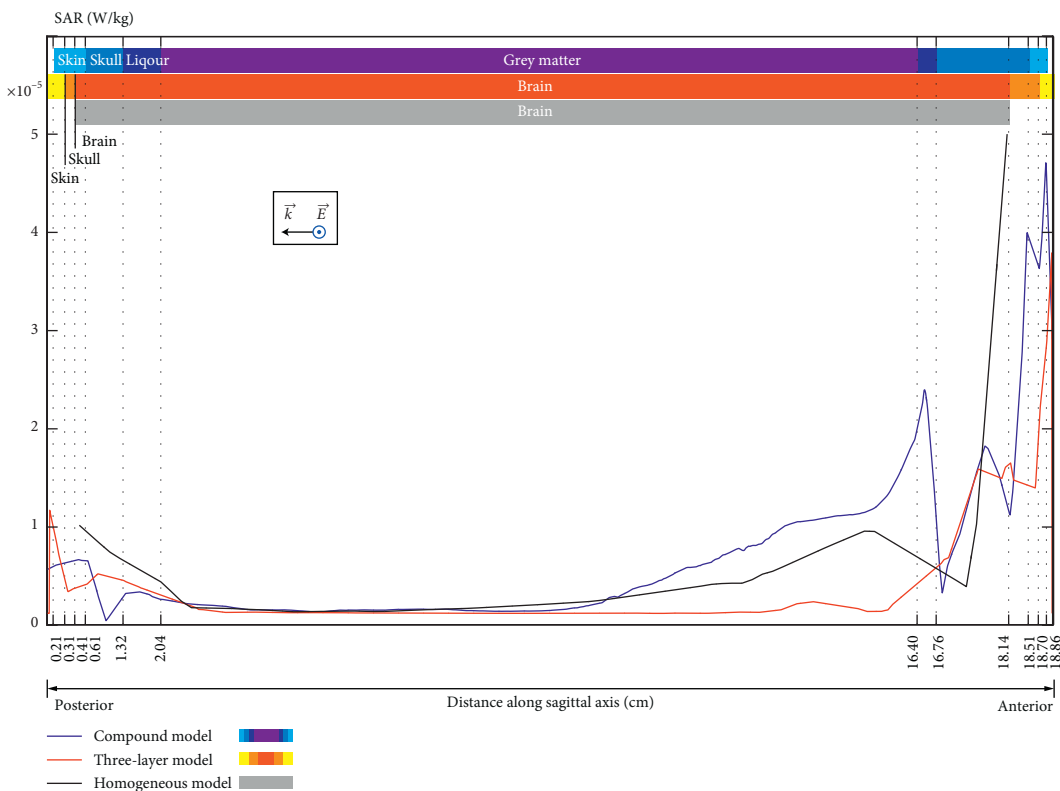


FIGURE 13: Comparison of the induced SAR along the sagittal axis of the homogeneous, the three-compartment, and the compound models, respectively, due to 1.8 GHz EM wave, horizontal polarization, incident on the anterior side.

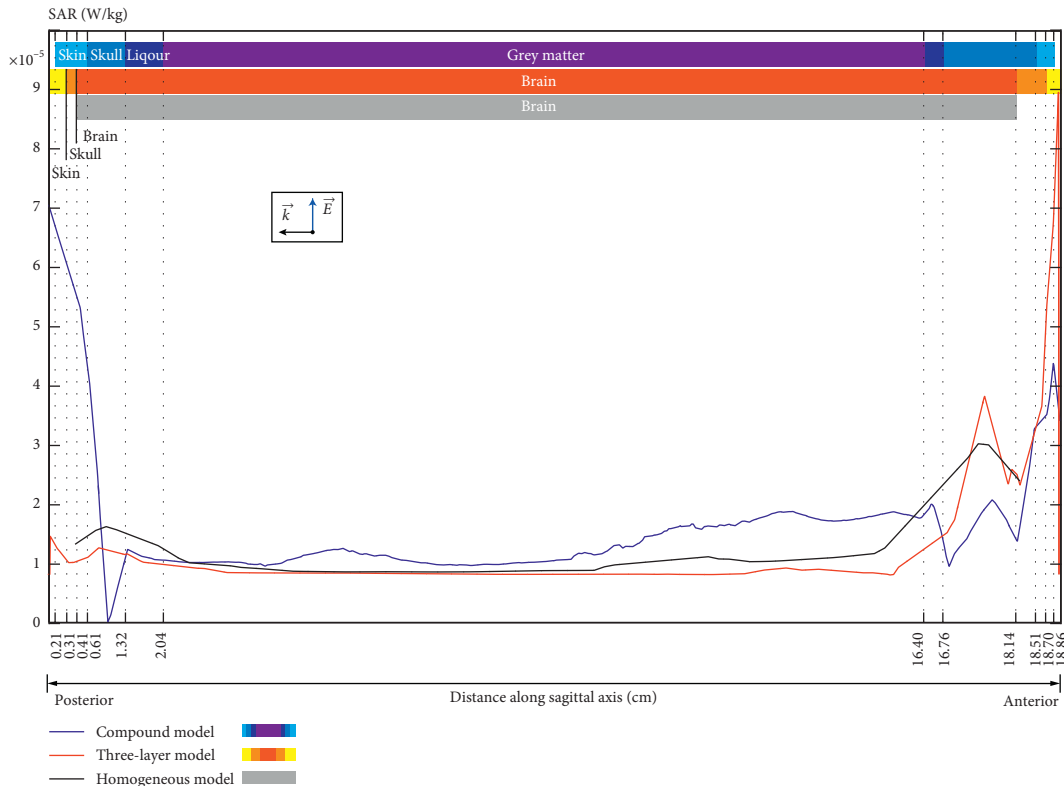


FIGURE 14: Comparison of the induced SAR along the sagittal axis of the homogeneous, the three-compartment, and the compound models, respectively, due to 1.8 GHz EM wave, vertical polarization, incident on the anterior side.

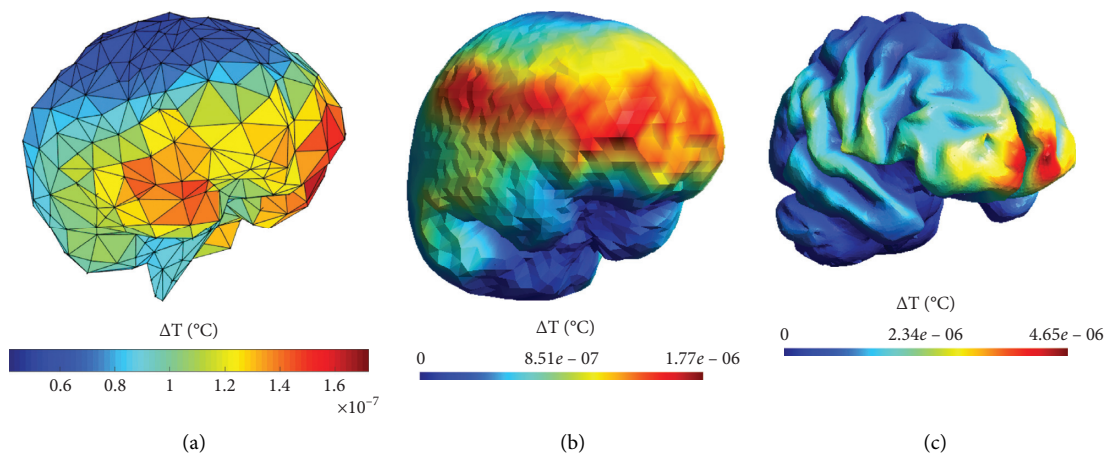


FIGURE 15: Temperature increase on the brain surface due to 900 MHz horizontally polarized EM wave: (a) homogeneous model, (b) three-compartment model, and (c) compound model.

Figures 15–18 show the results of the temperature increase on the surface of brain tissue in case of four different exposure scenarios. As evident from Figures 15–18, the highest value of temperature rise in the brain is obtained in the anterior region where the electromagnetic wave is impinging the brain model. In all four considered cases, similar distribution of temperature rise in the brain can be seen, as was expected from the SAR results. The maximum values obtained in all three models were similar, with the highest

one achieved using the compound model and the lowest one obtained with the homogeneous model. Although the two smoothed models lack the anatomical features of the compound model, they could still be considered useful in the rapid thermal dosimetry assessment, e.g., in quickly finding the location where the so-called hot-spots will be formed.

However, the obtained temperature rise in two smoothed models was significantly lower than the compound model, as evidenced more clearly in Figures 19–22.

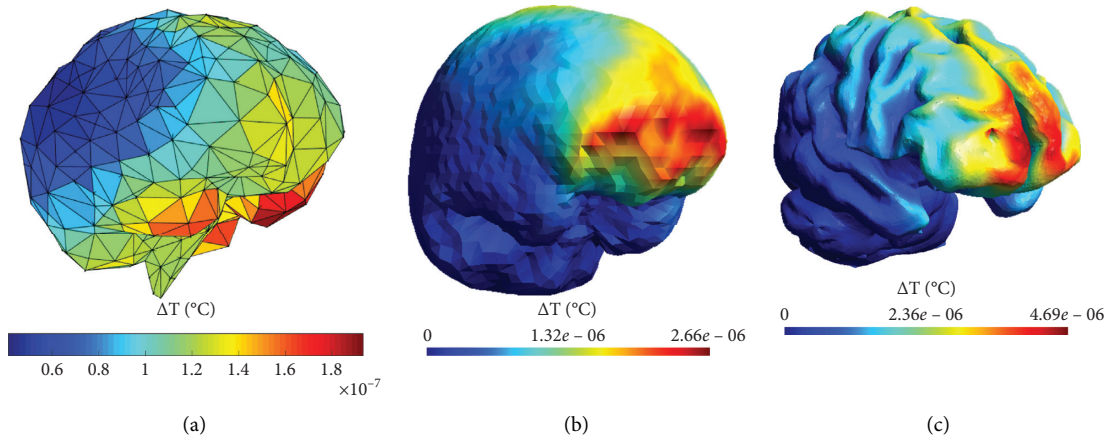


FIGURE 16: Temperature increase on the brain surface due to 900 MHz vertically polarized EM wave: (a) homogeneous model, (b) three-compartment model, and (c) compound model.

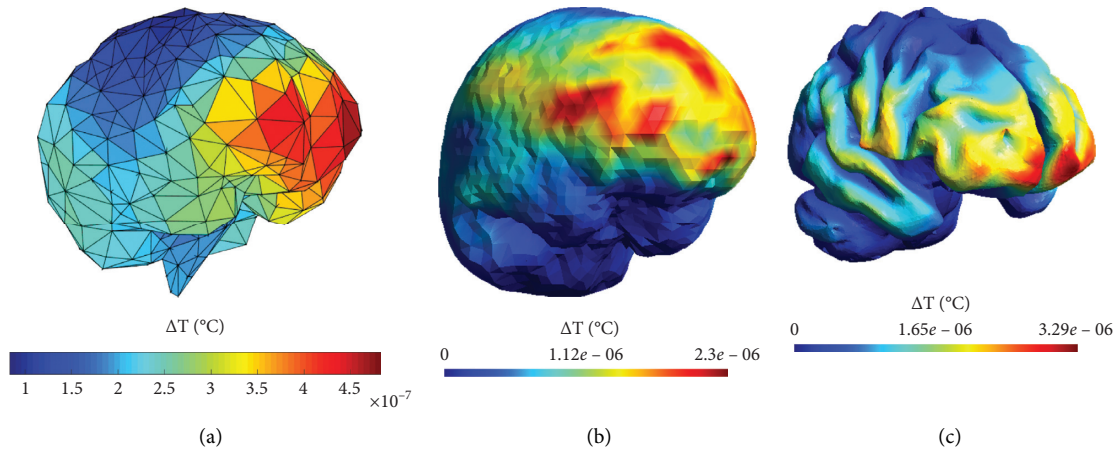


FIGURE 17: Temperature increase on the brain surface due to 1.8 GHz horizontally polarized EM wave: (a) homogeneous model, (b) three-compartment model, and (c) compound model.

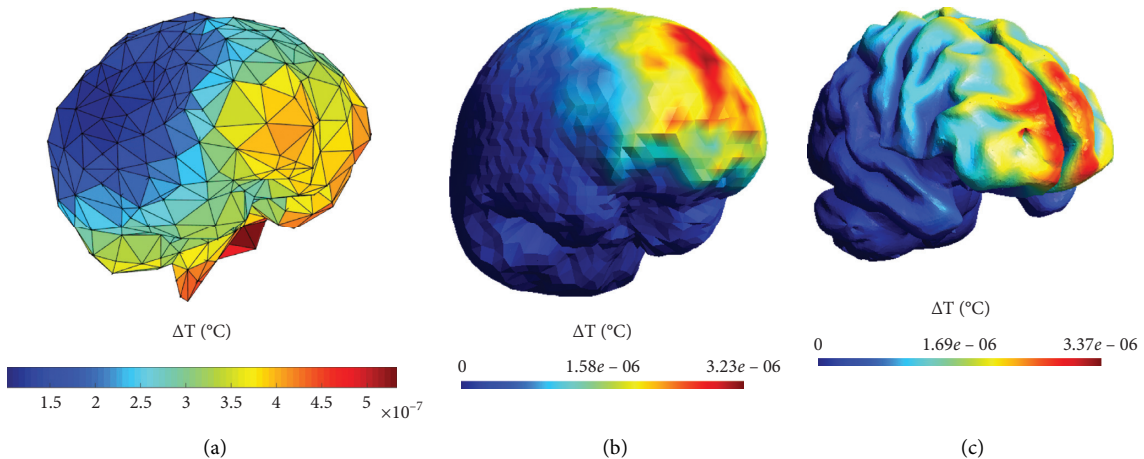


FIGURE 18: Temperature increase on the brain surface due to 1.8 GHz vertically polarized EM wave: (a) homogeneous model, (b) three-compartment model, and (c) compound model.

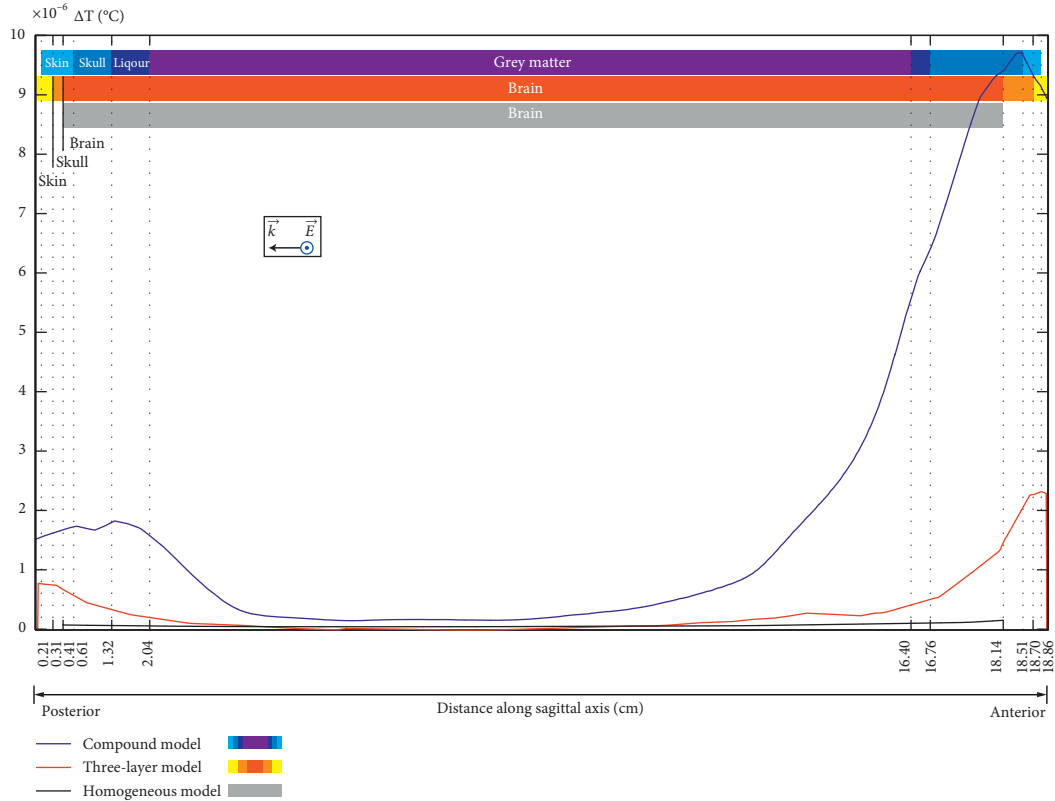


FIGURE 19: Comparison of the temperature increase along the sagittal axis of the homogeneous, the three-compartment, and the compound models, respectively, due to 900 MHz EM wave, horizontal polarization, incident on the anterior side.

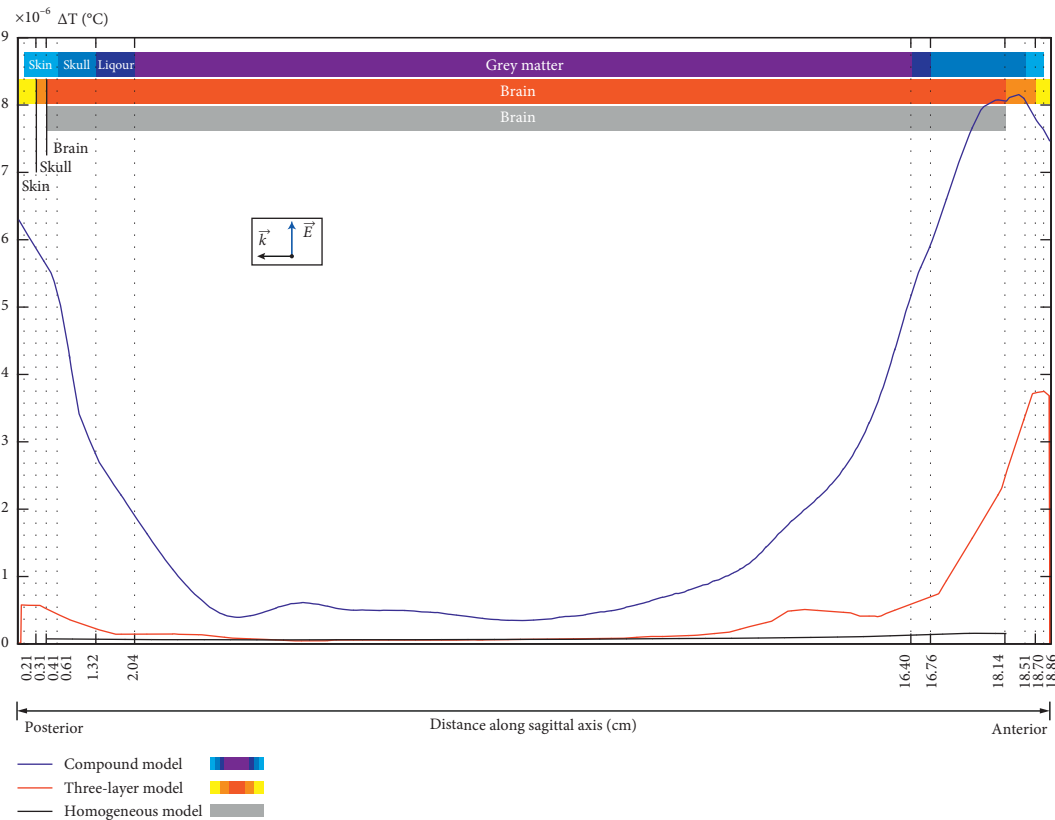


FIGURE 20: Comparison of the temperature increase along the sagittal axis of the homogeneous, the three-compartment, and the compound models, respectively, due to 900 MHz EM wave, vertical polarization, incident on the anterior side.

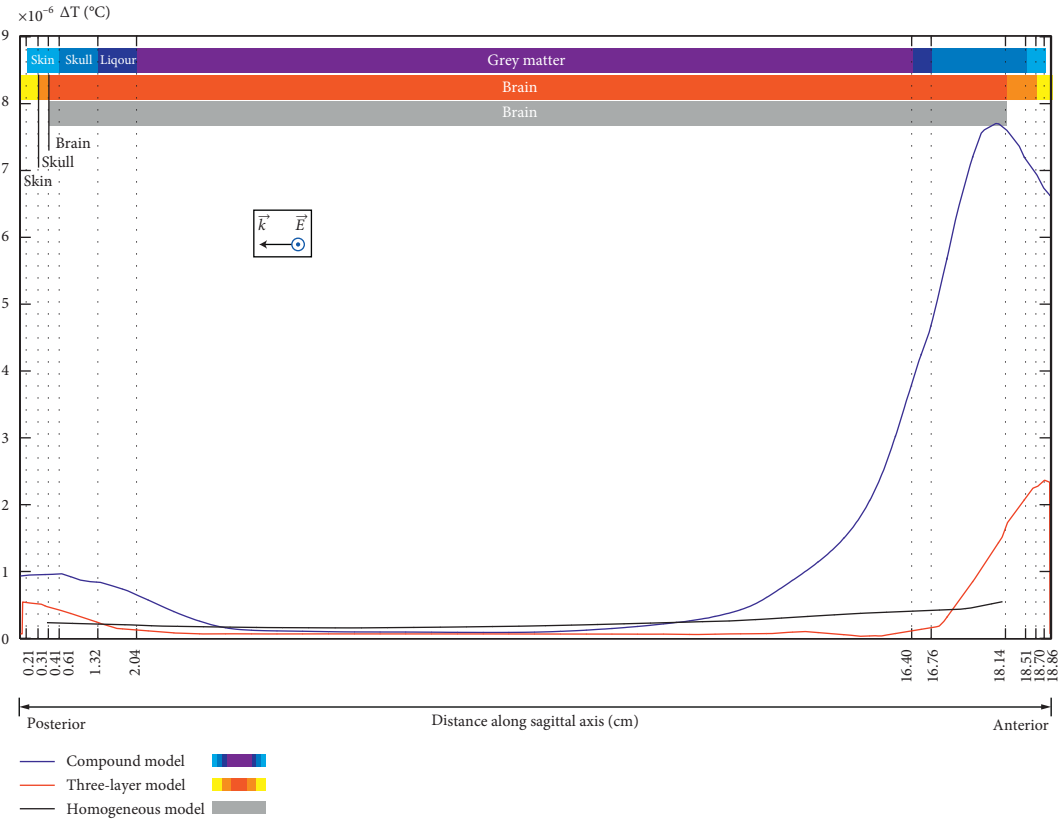


FIGURE 21: Comparison of the temperature increase along the sagittal axis of the homogeneous, the three-compartment, and the compound models, respectively, due to 1.8 GHz EM wave, horizontal polarization, incident on the anterior side.

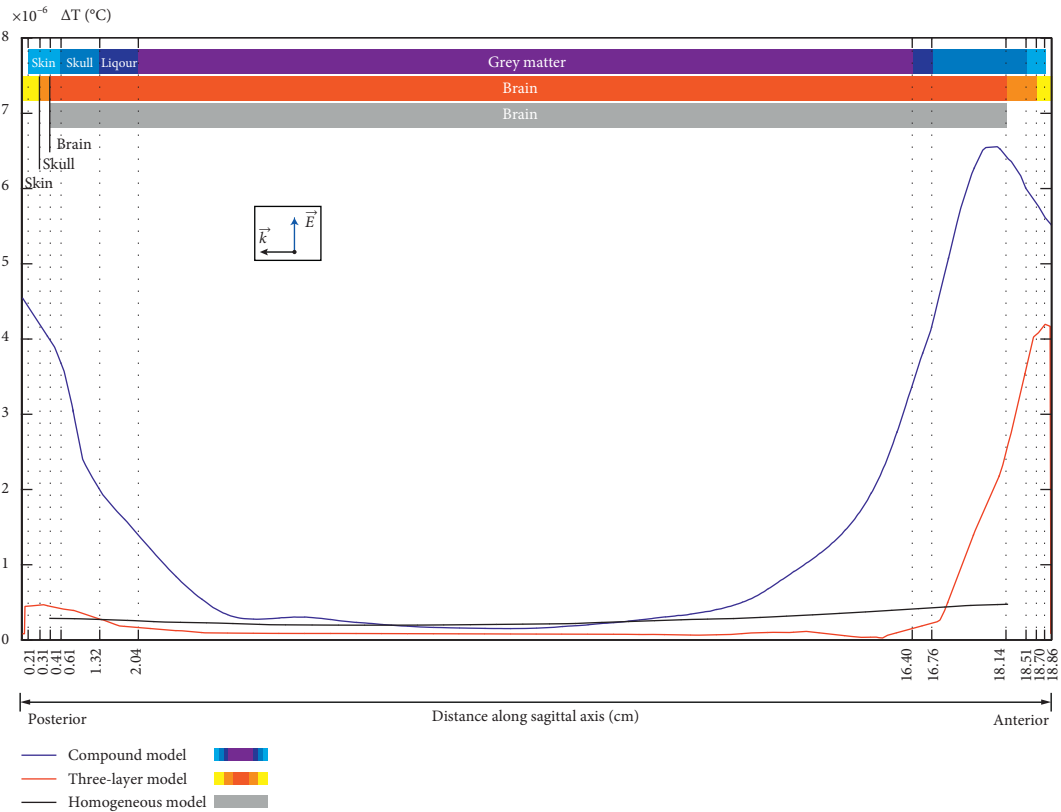


FIGURE 22: Comparison of the temperature increase along the sagittal axis of the homogeneous, the three-compartment, and the compound models, respectively, due to 1.8 GHz EM wave, vertical polarization, incident on the anterior side.

This could be attributed to higher heat exchange between the brain tissue and its surroundings, particularly in case of single-tissue model. In case of a multitissue models, the additional tissues surrounding the brain act as the additional insulating layer. The analysis of parameter variation in the three-compartment head model carried out by the stochastic collocation method [21] found that the brain parameters has the most significant influence on fields induced inside the brain. The homogeneous model, on the other hand, uses the concept of the effective surface heat transfer coefficient to take this into account [30]. The sensitivity analysis of this parameter and its influence on the temperature distribution in the human brain carried out in [30] found that along with the blood perfusion rate, the effective heat transfer coefficient has the most significant effect on the temperature rise.

Finally, scaling the induced electric field and the resulting SAR, the absorbed electromagnetic power,  $Q_{\text{SAR}}$ , can be determined using  $Q_{\text{SAR}} = \rho \text{SAR}_{\text{max}}$ , where  $\rho$  is the brain density given in Table 2. The values for  $Q_{\text{SAR}}$  in addition to  $\text{SAR}_{\text{max}}$  are given in Table 4.

Taking into account the average heat generated by the metabolism,  $Q_m = 6385 \text{ W/m}^3$  [30], as evident from Table 4, the amount of heat generated per unit time per unit volume due to absorption of EM energy in the brain is found negligible. The increase of  $Q_{\text{SAR}}$  to the levels of  $Q_m$ , according to [30], would result in the comparable average temperature rise as well as the maximum temperature rise of  $0.1^\circ\text{C}$ .

#### 4. Conclusion

This paper presents the thermal analysis comparison in the extracted or the single organ models of the human eye and the brain, and the compound models incorporated into the detailed human head, respectively. For each organ (human eye and human brain), four different scenarios have been considered, related to high-frequency electromagnetic exposure at two different frequencies and two polarizations.

Although the numerical results for the two human eye models in general showed similar SAR distributions as well as comparable temperature rise, there are also some obvious differences. Namely, the extracted eye model, due to model symmetrical features when considering the frontally incident plane wave, produced practically the same results for both polarizations, compared to the compound model. Moreover, the results suggest that the extracted eye model underestimates the temperature rise, as the air surrounding the eye will facilitate a better heat exchange, than the compound model, where the influence of the surrounding head tissues perfused by blood will reduce this heat exchange between the eye itself and the surroundings. On the other hand, the compound eye model showed the reduced values of SAR in the crystalline lens while not having the effect on the distribution in the adjacent ocular tissues. This result indicates the possibility of omitting the detailed lens modeling, such as in a case when electromagnetic power deposition only in the superficial eye regions is of interest.

Moreover, similar distributions of SAR and the temperature rise have been obtained using different brain

models, i.e., homogeneous, three-compartment, and compound one, respectively. It has been shown that the peak SAR value obtained in all three brain models does not exceed the limit set as the basic restriction for localized SAR, for the occupational exposure. Furthermore, the assessment of the resultant temperature rise in all models suggests that the resultant temperature rise should not exceed  $0.1^\circ\text{C}$ .

Finally, as a more general remark, the use of a geometrically appreciable simpler models such as the three-compartment model, or even the homogeneous model, lacking many of the anatomical features present in the compound model, may be found useful in the rapid thermal dosimetry assessment. Following the initial assessment, the more elaborate models, featuring additional tissues and more finer anatomical features, could be used later, focusing on the particular model details.

#### Data Availability

The data used to support the findings of this study are available from the corresponding author upon request.

#### Conflicts of Interest

The authors declare that they have no conflicts of interest.

#### Acknowledgments

The authors would like to thank I. Laakso from Aalto University, Finland, and A. Hirata from Nagoya Institute of Technology, Japan, for providing the detailed head model, and also, A. Hunold and J. Haueisen from TU Ilmenau, Germany, for providing the three-compartment head model.

#### References

- [1] International Commission on Non-Ionizing Radiation Protection (ICNIRP), "Guidelines for limiting exposure to electromagnetic fields (100 kHz to 300 GHz)," *Health Physics*, vol. 118, no. 5, pp. 483–524, 2020.
- [2] J. W. Hand, "Modelling the interaction of electromagnetic fields (10 MHz–10 GHz) with the human body: methods and applications," *Physics in Medicine and Biology*, vol. 53, no. 16, pp. R243–R286, 2008.
- [3] D. Poljak, "Electromagnetic fields: environmental exposure," in *Encyclopedia of Environmental Health*, pp. 259–268, Elsevier, Amsterdam, Netherlands, 2011.
- [4] D. Poljak, M. Cvetković, H. Dodig, and A. Peratta, "Electromagnetic-thermal analysis for human exposure to high frequency (HF) radiation," *International Journal of Design & Nature and Ecodynamics*, vol. 12, no. 1, pp. 55–67, 2017.
- [5] D. Poljak and M. Cvetković, *Human Interaction with Electromagnetic Fields: Computational Models in Dosimetry*, Academic Press, Cambridge, MA, USA, 2019.
- [6] D. Poljak, *Human Exposure to Electromagnetic Fields*, WIT Press, Southampton, UK, 2003.
- [7] K. D. Singh, N. S. Logan, and B. Gilmartin, "Three-dimensional modeling of the human eye based on magnetic resonance imaging," *Investigative Ophthalmology & Visual Science*, vol. 47, no. 6, pp. 2272–2279, 2006.
- [8] T. Nagaoka, S. Watanabe, K. Sakurai et al., "Development of realistic high-resolution whole-body voxel models of Japanese

- adult males and females of average height and weight, and application of models to radio-frequency electromagnetic-field dosimetry," *Physics in Medicine and Biology*, vol. 49, no. 1, pp. 1–15, 2003.
- [9] M. Caon, "Voxel-based computational models of real human anatomy: a review," *Radiation and Environmental Biophysics*, vol. 42, no. 4, pp. 229–235, 2004.
- [10] M. J. Ackerman, "The visible human project," *Proceedings of the IEEE*, vol. 86, no. 3, pp. 504–511, 1998.
- [11] J. W. Massey and A. E. Yilmaz, "AustinMan and Austin-Woman: high-fidelity, anatomical voxel models developed from the VHP color images," in *Proceedings of the 2016 38th Annual International Conference of the IEEE Engineering in Medicine and Biology Society (EMBC)*, pp. 3346–3349, Orlando, FL, USA, August 2016.
- [12] D. Poljak, S. Šesnić, M. Cvetković et al., "Stochastic collocation applications in computational electromagnetics," *Mathematical Problems in Engineering*, vol. 2018, Article ID 1917439, 13 pages, 2018.
- [13] P. Kersaudy, B. Sudret, N. Varsier, O. Picon, and J. Wiart, "A new surrogate modeling technique combining Kriging and polynomial chaos expansions - application to uncertainty analysis in computational dosimetry," *Journal of Computational Physics*, vol. 286, pp. 103–117, 2015.
- [14] L. Golestani-rad, M. Mattes, J. R. Mosig, and C. Pollo, "Effect of model accuracy on the result of computed current densities in the simulation of transcranial magnetic stimulation," *IEEE Transactions on Magnetics*, vol. 46, no. 12, pp. 4046–4051, 2010.
- [15] M. Cvetković, H. Dodig, and D. Poljak, "A study on the use of compound and extracted models in the high frequency electromagnetic exposure assessment," *Mathematical Problems in Engineering*, vol. 2017, Article ID 7932604, 12 pages, 2017.
- [16] H. Dodig, S. Lalléchère, P. Bonnet, D. Poljak, and K. El Khamlichi Drissi, "Stochastic sensitivity of the electromagnetic distributions inside a human eye modeled with a 3D hybrid BEM/FEM edge element method," *Engineering Analysis with Boundary Elements*, vol. 49, pp. 48–62, 2014.
- [17] M. Cvetković and D. Poljak, "An efficient integral equation based dosimetry model of the human brain," in *Proceedings of 2014 International Symposium on Electromagnetic Compatibility (EMC EUROPE) 2014*, pp. 375–380, Gothenburg, Sweden, September 2014.
- [18] S. M. Blinkov and I. I. Glezer, *The Human Brain in Figures and Tables. A Quantitative Handbook*, Plenum Press, New York, NY, USA, 1968.
- [19] D. Poljak, M. Cvetković, O. Bottauscio et al., "On the use of conformal models and methods in dosimetry for non-uniform field exposure," *IEEE Transactions on Electromagnetic Compatibility*, vol. 60, no. 2, pp. 327–337, 2018.
- [20] M. Stenroos, A. Hunold, and J. Hauelsen, "Comparison of three-shell and simplified volume conductor models in magnetoencephalography," *Neuroimage*, vol. 94, pp. 337–348, 2014.
- [21] A. Šušnjara, H. Dodig, M. Cvetković, and D. Poljak, "Stochastic dosimetry of a three compartment head model," *Engineering Analysis with Boundary Elements*, vol. 117, pp. 332–345, 2020.
- [22] I. Laakso, S. Tanaka, S. Koyama, V. De Santis, and A. Hirata, "Inter-subject variability in electric fields of motor cortical tDCS," *Brain Stimulation*, vol. 8, no. 5, pp. 906–913, 2015.
- [23] D. Poljak, D. Cavka, H. Dodig, C. Peratta, and A. Peratta, "On the use of the boundary element analysis in bioelectromagnetics," *Engineering Analysis with Boundary Elements*, vol. 49, pp. 2–14, 2014.
- [24] H. Dodig, D. Poljak, and A. Peratta, "Hybrid BEM/FEM edge element computation of the thermal rise in the 3D model of the human eye induced by high frequency EM waves," in *Proceedings of the 2012 20th International Conference on Software, Telecommunications and Computer Networks (SoftCOM)*, IEEE, Split, Croatia, pp. 1–5, September 2012.
- [25] D. Poljak, M. Cvetković, A. Peratta, C. Peratta, H. Dodig, and A. Hirata, "On some integral approaches in electromagnetic dosimetry," in *Proceedings of the BioEM 2016*, pp. 289–296, Ghent, Belgium, June 2016.
- [26] M. Cvetkovic, D. Poljak, and J. Hauelsen, "Analysis of transcranial magnetic stimulation based on the surface integral equation formulation," *IEEE Transactions on Biomedical Engineering*, vol. 62, no. 6, pp. 1535–1545, 2015.
- [27] H. H. Pennes, "Analysis of tissue and arterial blood temperatures in the resting human forearm," *Journal of Applied Physiology*, vol. 85, no. 1, pp. 5–34, 1948.
- [28] D. Poljak, A. Peratta, and C. A. Brebbia, "The boundary element electromagnetic-thermal analysis of human exposure to base station antennas radiation," *Engineering Analysis with Boundary Elements*, vol. 28, no. 7, pp. 763–770, 2004.
- [29] M. Cvetković, H. Dodig, and D. Poljak, "Numerical comparison of compound and extracted eye models for high frequency dosimetry," *International Journal for Engineering Modelling*, vol. 31, no. 1-2, pp. 1–13, 2018.
- [30] M. Cvetković, D. Poljak, and A. Hirata, "The electromagnetic-thermal dosimetry for the homogeneous human brain model," *Engineering Analysis with Boundary Elements*, vol. 63, pp. 61–73, 2016.
- [31] A. L. Sukstanskii and D. A. Yablonskiy, "Theoretical model of temperature regulation in the brain during changes in functional activity," *Proceedings of the National Academy of Sciences*, vol. 103, no. 32, pp. 12144–12149, 2006.
- [32] A. Hirata, S.-I. Matsuyama, and T. Shiozawa, "Temperature rises in the human eye exposed to EM waves in the frequency range 0.6–6 GHz," *IEEE Transactions on Electromagnetic Compatibility*, vol. 42, no. 4, pp. 386–393, 2000.
- [33] O. Fujiwara and A. Kato, "Computation of sar inside eyeball for 1.5-GHz microwave exposure using finite-difference time-domain technique," *IEICE Transactions on Communications*, vol. 77, no. 6, pp. 732–737, 1994.
- [34] D. Poljak and M. Cvetković, "On the incident power density calculation in GHz frequency range: a case of Hertz dipole," in *Proceedings of the 2019 4th International Conference on Smart and Sustainable Technologies (SpliTech)*, IEEE, Split, Croatia, pp. 1–4, June 2019.
- [35] M. Cvetković, H. Dodig, and D. Poljak, "Temperature increase in the extracted and compound eye models," in *Proceedings of the 2017 25th International Conference on Software, Telecommunications and Computer Networks (SoftCOM)*, pp. 1–6, IEEE, Split, Croatia, September 2017.
- [36] International Commission on Non-Ionizing Radiation Protection (ICNIRP), "Guidelines for limiting exposure to time-varying electric, magnetic and electromagnetic fields (up to 300 GHz)," *Health Physics*, vol. 74, no. 4, pp. 494–522, 1998.